INDIAN JOURNAL OF SCIENCE AND TECHNOLOGY

ORIGINAL ARTICLE

OPEN ACCESS

Received: 09/02/2025

Accepted: 14/05/2025

Published: 10/06/2025

Citation: Premalatha M, Anitha K, Revathi B, Balachandran V, Narayana B, Jayashree A, Thirughanasambantham N (2025) Molecular Structure, Vibrational Analysis, and Pharmacokinetic Evaluation of a Novel Pyrazole Derivative: Experimental and Computational Study. Indian Journal of Science and Technology 18(21): 1662-1680. https://doi.org/10.17485/IJST/v18i21.276

* **Corresponding author**.

brevathi1965@gmail.com

Funding: None

Competing Interests: None

Published By Indian Society for Education and Environment (iSee)

ISSN
Print: 0974-6846
Electronic: 0974-5645

Molecular Structure, Vibrational Analysis, and Pharmacokinetic Evaluation of a Novel Pyrazole Derivative: Experimental and Computational Study

M. Premalatha[1], K. Anitha[2], B. Revathi[3]*, V. Balachandran[3], B. Narayana[4], A. Jayashree[5], N. Thirughanasambantham[3]

1 Department of Physics, Shrimati Indira Gandhi College (affiliated to Bharathidasan University) Tiruchirapalli 620 002, Tamil Nadu, India
2 Department of Physics Government Arts and Science College (affiliated to Bharathidasan University) Lalgudi 621712, India
3 Centre for Research, Department of Physics, Arignar Anna Government Arts College (affiliated to Bharathidasan University), Musiri, Tiruchirapalli 621211, India
4 K K University, Bihar Sherif, Berauti, Bihar 803115, India
5 Department of Studies in Chemistry, Mangalore University, Mangalagangotri 574 199, Mangaluru, Karnataka, India

Abstract

Objectives: To synthesize the novel compound 5-Amino-3-(4-cyanophenyl)-1-isonicotinoyl-2,3-dihydro-1H-pyrazole-4-carbonitrile (ACIDPC) and perform a comprehensive spectroscopic characterization to evaluate its structural, vibrational, and electronic properties. **Methods:** The ACIDPC compound was synthesized via an ultrasound-assisted synthesis protocol. Computational analyses were performed using molecular docking software. Spectroscopic and analytical characterizations were carried out using Fourier-transform infrared (FT-IR) spectroscopy, Fourier-transform Raman (FT-Raman) spectroscopy, ultraviolet-visible (UV-Vis) spectrophotometry, nuclear magnetic resonance (NMR) spectroscopy, and antimicrobial activity assays. **Findings:** Molecular stability analysis revealed that interactions between the lone pairs of N33 and N1 with the π^* orbitals, particularly in the C4-C5 and C6-C7 regions, play a crucial role in stabilizing the ACIDPC molecule. The calculated dipole moment of 6.15 Debye suggests strong binding affinity, indicating potential for effective molecular interactions with target receptors. Drug-like properties were assessed, with a bioavailability score of 0.55 indicating favorable pharmacological relevance. Molecular docking studies with proteins, including insulin inhibitor (PDB ID: 2CI2), antimicrobial protein (PDB ID: 2EA9), and antineoplastic protein (PDB ID: 6kLK), demonstrated stable complexes with binding affinities of -6.67, -7.33, and -7.74 kcal/mol, respectively. **Novelty:** To the best of our knowledge, the novel ACIDPC compound synthesized in this study has not been reported elsewhere. Its molecular docking studies, along with optical characterization, make this research unique.

Keywords: Pyrazole; Antimicrobial activity; Insulin inhibitor; Antineoplastic activity; Drug-likeness; ADMET

1 Introduction

Pyrazole-based scaffolds have emerged as vital constituents in the field of medicinal chemistry due to their favorable physicochemical and pharmacological properties. The pyrazole ring is notable for its ability to engage in hydrogen bonding, dipole–dipole, and $\pi-\pi$ stacking interactions, which contribute to the enhanced molecular recognition and binding affinity of drug candidates[(1)],[(2)],[(3)]. Additionally, pyrazole derivatives exhibit high dipole moments and favorable solubility profiles, further supporting their role in the development of therapeutically relevant molecules. The incorporation of pyrazole moieties into drug frameworks has led to the discovery of compounds with diverse biological activities, including antiviral, anti-inflammatory, analgesic[(4)], antipyretic[(5)], anticoagulant[(6)], antiobesity[(7)], and antineoplastic effects[(8)]. These activities are often attributed to the ability of pyrazole derivatives to interact selectively with various protein targets, influencing key signaling pathways implicated in both chronic and infectious diseases. In particular, 2, 3-dihydropyrazole derivatives have demonstrated enhanced biological efficacy, with reported antioxidant, antimicrobial, and anticancer properties[(6)],[(9)].

Despite growing interest, prior studies have often been limited in scope, focusing primarily on basic structural characterization methods such as Nuclear magnetic resonance (NMR) and elemental analysis, while neglecting comprehensive quantum chemical and pharmacokinetic evaluations[(6)],[(9)]. This lack of detailed structural and functional insight restricts the broader application and optimization of pyrazole derivatives in drug discovery.

In response to this gap, the present study aims to provide a comprehensive structural, electronic, and pharmacokinetic characterization of the compound ACIDPC, a novel dihydropyrazole-based molecule. To our knowledge, this is the first investigation to integrate multiple quantum chemical descriptors—including Highest occupied molecular orbital (HOMO)–Lowest unoccupied molecular orbital (LUMO), natural bond orbital (NBO), molecular electrostatic potential (MEP), electron localization function (ELF), localized orbital locator (LOL), noncovalent interactions (NCI), and Fukui function analyses—with molecular docking and Adsorption, Distribution, Metabolism, Excretion and Toxicity (ADME/Tox) profiling for this compound class.

The central objective of this study is to evaluate the electronic reactivity and drug-like behavior of ACIDPC and to explore its potential as a multi-target therapeutic agent. The compound's unique electronic architecture, characterized by the presence of both electron-donating and electron-withdrawing groups, is hypothesized to create a multifunctional electrostatic environment conducive to selective biological interactions. Favorable docking scores and ADMET parameters further suggest that ACIDPC may serve as a promising candidate for antimicrobial, antineoplastic, and insulin-inhibitory applications.

Thus, this work introduces a structurally and electronically novel pharmacophore and provides foundational insights for future exploration of ACIDPC and related derivatives in therapeutic development.

2 Methodology

2.1 Synthesis and comprehensive characterization of ACIDPC compound

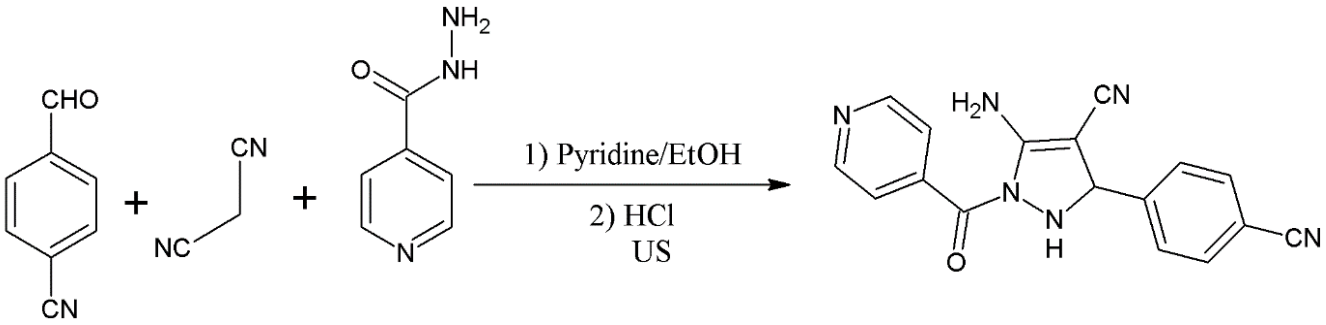

A mixture of 4-cyanobenzaldehyde (0.131 g, 1 mmol), malononitrile (0.066 g, 1 mmol), and a catalytic amount of pyridine was dissolved in 5 mL of ethanol and subjected to sonication at 60 W for 10 minutes. Subsequently, isoniazid (0.138 g, 1 mmol) and 5 drops of dilute HCl were added to the reaction mixture, and sonication was continued for an additional 30–40 minutes. The reaction progress was monitored by thin-layer chromatography (TLC). Upon completion, the reaction mixture was poured onto crushed ice and stirred thoroughly. The resulting precipitate was collected by filtration, washed with distilled water, and purified by column chromatography using a 7:3 ethyl acetate:hexane eluent system. The final product was obtained as a pale-yellow solid with a yield of 75% after 30 minutes and a melting point of 196–198 °C.

2.2 Experimental Methods

Fourier-transform infrared (FT-IR) and Fourier-transform Raman (FT-Raman) spectra of ACIDPC were recorded to investigate its vibrational characteristics. The FT-IR spectrum was obtained using a Bruker IFS 66V spectrometer in the spectral range of 4000–400 cm^{-1}, while the FT-Raman spectrum was measured on a Bruker RFS 100/S spectrometer equipped with an Nd:YAG laser source (wavelength: 1064 nm, power output: 150 mW), covering a range of 4000–50 cm^{-1}. All spectra were acquired from solid-state samples under ambient conditions. ^{6}H and ^{13}C NMR spectra were recorded using a Bruker Avance III 400 MHz spectrometer. The compound was dissolved in deuterated dimethyl sulfoxide (DMSO-d_6), and tetramethylsilane (TMS) was used as an internal standard. Chemical shifts (δ) were reported in parts per million (ppm), and the signal multiplicities were denoted as singlet (s), doublet (d), triplet (t), or multiplet (m). Coupling constants (J) were provided in hertz (Hz), along with the corresponding number of protons. Ultraviolet-visible absorption spectra were obtained using a Perkin-Elmer Lambda 35 UV-Visible spectrometer. Measurements were carried out at room temperature using ethanol as the solvent, with spectra recorded over the wavelength range of 190–1100 nm. The molecular mass of ACIDPC was confirmed through liquid chromatography–mass spectrometry (LC-MS) using a Shimadzu LCMS 2010 system. The analysis was performed to validate the molecular structure and purity of the synthesized compound.

2.3 Computational Methods

All quantum chemical calculations were performed using the Gaussian 09W software package [10], with molecular visualizations conducted via GaussView 5.0 [11]. The molecular structure of ACIDPC was optimized using Density Functional Theory (DFT) at the B3LYP/cc-PVDZ and B3LYP/cc-PVTZ levels of theory. Vibrational frequencies were calculated to confirm the stability of the optimized structures (absence of imaginary frequencies), and scaling factors were applied to align theoretical data with experimental spectra. Time-dependent DFT (TD-DFT) calculations were employed to evaluate electronic transitions both in the gas phase and in ethanol, providing insights into the compound's optical behavior. Natural Bond Orbital (NBO) analysis was conducted using NBO 3.1 [12] to assess intramolecular donor–acceptor interactions and charge delocalization. Potential Energy Distribution (PED) assignments for vibrational modes were made using VEDA 4 [13]. Further topological analyses, including Electron Localization Function (ELF) and Localized Orbital Locator (LOL), were performed using Multiwfn 3.7 to investigate bonding characteristics and electron density distribution. To explore the biological activity of ACIDPC, molecular docking simulations were carried out using AutoDockTools (ADT) version 4.2.6 [14]. The PASS (Prediction of Activity Spectra for Substances) analysis guided the selection of potential targets. Three relevant proteins were selected for docking based on their biological significance:

- Insulin inhibitor – PDB ID: 2CI2
- Antimicrobial target – PDB ID: 2EA9
- Antineoplastic target – PDB ID: 6KLK

The compound's binding affinities and interaction sites were evaluated to determine its potential as a multi-target therapeutic agent. An in silico ADME/Tox evaluation was performed to predict the absorption, distribution, metabolism, excretion, and toxicity profiles of ACIDPC. These parameters were assessed to validate its drug-likeness and potential for further development as a pharmacologically active compound.

3 Results and Discussion

3.1 Structural characterization of novel ACIDPC

The ACIDPC structure was optimized at the B3LYP/cc-PVDZ and B3LYP/cc-PVTZ levels (Gaussian 09W, Table 1), and the atom numbering is illustrated in Figure 1. Without crystallographic data, the computed geometry was validated against structurally related molecules [15]. The N1–N2 bond in the ACIDPC pyrazole ring measures 1.43 Å, exceeding the typical 1.374 Å reported for related systems, likely due to the electron-withdrawing C=O group at N1. Consistent across both basis sets, bond lengths include N1–C6 (1.39/1.38 Å), N1–C5 (1.42/1.41 Å), N11–C12 (1.34/1.33 Å), N11–C10 (1.16/1.15 Å), N29–C28 (1.17/1.16 Å), and N33–C32 (1.17/1.16 Å). The N34–H35 and N34–H36 bond lengths are 1.01/1.01 Å and 1.02/1.01 Å, respectively. The aromatic C–C bond lengths (1.39–1.40 Å) align with reported values [16].

Bond angle analysis underscores the conformational features of ACIDPC. For example, bond angles at C20, such as C3–C20–C21 (121.63°/121.83°), align with reported values. Significant pyrazole ring angles include N2–N1–C5 (132.7°), N2–N1–C6 (111.8°), and C5–N1–C6 (125.6°), along with N1–C5–C4 (139.4°) and N1–C5–N34 (107.3°) at adjacent positions. Bond angles

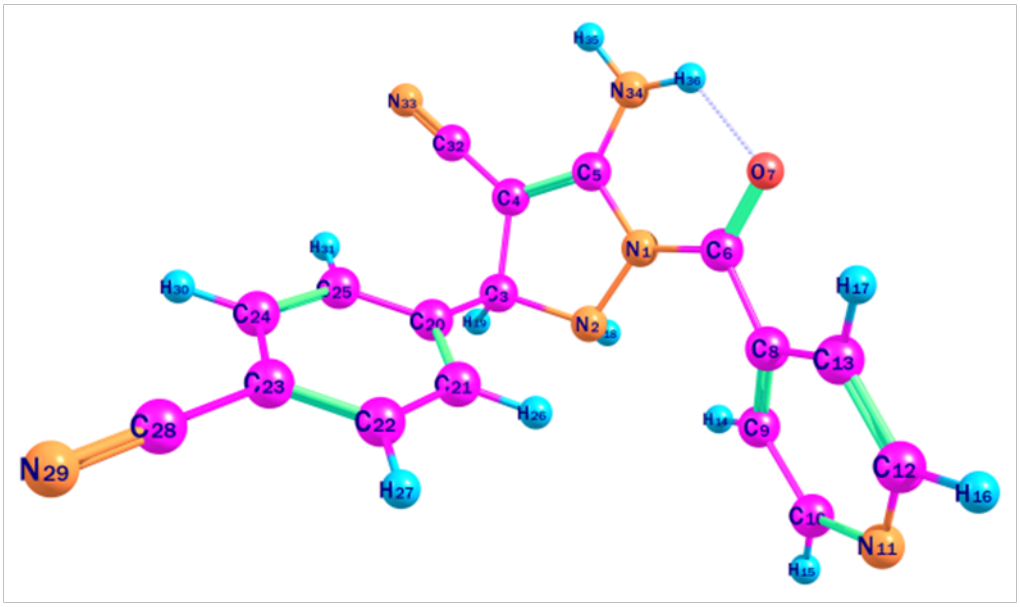

Fig 1. Optimised geometry of 5-Amino-3-(4-cyanophenyl)-1-isonicotinoyl-2,3-dihydro-1H-pyrazole-4-carbonitrile

such as C6–C8–C9, C6–C8–C13, and C9–C8–C13 deviate from ideal tetrahedral values, likely due to steric hindrance between the pyridine ring and the C8 carbonyl group. The torsional profile further elucidates ACIDPC's 3D conformation. Torsion angles (e.g., C3–C20–C21–H26, C3–C20–C25–C24) indicate non-planarity between pyrazole and pyridine rings. Further torsions (e.g., N2–N1–C5–N34, N2–N1–C6–O7) highlight pyrazole interactions with nearby substituents. Torsions (N1–C5–N34–H35, N1–C5–N34–H36) confirm the amino group's out-of-plane orientation, stabilized by an intramolecular C6–O7···H36 hydrogen bond.

Table 1. Optimized geometrical parameters of 5-Amino-3-(4-cyanophenyl)-1-isonicotinoyl-2,3-dihydro-1*H*-pyrazole-4-carbonitrile at B3LYP method with B3LYP /cc-pVDZ and B3LYP /cc-pVTZ level

Bond length(Å)			**Bond Angle(Å)**			**Dihedral angle(Å)**		
Parameter	**B3LYP/ cc-pVDZ**	**B3LYP/ cc-pVTZ**	**Parameter**	**B3LYP/ cc-pVDZ**	**B3LYP/ cc-pVTZ**	**Parameter**	**B3LYP/ cc-pVDZ**	**B3LYP/ cc-pVTZ**
N1-N2	1.43	1.43	N2-N1-C5	109.36	109.40	C5-N1-N2-C3	-21.13	-18.72
N1-C5	1.42	1.41	N2-N1-C6	123.80	123.08	C5-N1-N2-N18	90.73	94.76
N1-C6	1.39	1.38	C5-N1-C6	124.77	125.61	C6-N1-N2-C3	143.16	146.33
N2-C3	1.49	1.48	N1-N2-C3	105.39	105.73	C6-N1-N2-H18	-104.98	-100.18
N2-H18	1.02	1.01	N1-N2-H18	105.03	105.96	N2-N1-C5-C4	9.48	8.17
C3-C4	1.53	1.53	C3-N2-H18	106.14	107.12	N2-N1-C5-N34	-168.89	-170.42
C3-H19	1.10	1.09	N2-C3-C4	102.35	102.36	C6-N1-C5-C4	-154.62	-156.42
C3-C20	1.53	1.52	N2-C3-H19	107.13	107.23	C6-N1-C5-N34	27.01	24.99
C4-C5	1.37	1.36	N2-C3-C20	112.76	113.09	N2-N1-C6-O7	-171.95	-169.97

Continued on next page

Table 1 continued

C4-C32	1.41	1.40	C4-C3-H19	112.00	111.78	N2-N1-C6-C8	8.32	11.23
C5-N34	1.35	1.35	C4-C3-C20	113.96	113.85	C5-N1-C6-O7	-10.07	-7.38
C6-O7	1.23	1.22	H19-C3-C20	108.41	108.32	C5-N1-C6-C8	170.20	173.82
C6-C8	1.50	1.50	C3-C4-C5	108.30	108.72	N1-N2-C3-C4	23.17	20.67
C8-C9	1.40	1.39	C3-C4-C32	126.90	126.70	N1-N2-C3-H19	141.11	138.42
C8-C13	1.40	1.39	C5-C4-C32	124.54	124.39	N1-N2-C3-C20	-99.70	-102.25
C9-C10	1.40	1.39	N1-C5-C4	109.04	109.36	H18-N2-C3-C4	-87.91	-92.01
C9-H14	1.09	1.08	N1-C5-N34	120.69	120.62	H18-N2-C3-H19	30.04	25.74
C10-N11	1.34	1.33	C4-C5-N34	130.24	130.01	H18-N2-C3-C20	149.23	145.07
C10-H15	1.09	1.08	N1-C6-O7	120.13	121.07	N2-C3-C4-C5	-18.27	-16.53
N11-C12	1.34	1.33	N1-C6-C8	119.98	118.42	N2-C3-C4-C32	167.47	168.39
C12-C13	1.40	1.39	O7-C6-C8	119.89	120.51	H19-C3-C4-C5	-132.70	-130.99
C12-H16	1.09	1.08	C6-C8-C9	126.39	124.17	H19-C3-C4-C32	53.04	53.93
C13-H17	1.09	1.08	C6-C8-C13	115.92	117.58	C20-C3-C4-C5	103.78	105.87
C20-C21	1.40	1.39	C9-C8-C13	117.55	118.06	C20-C3-C4-C32	-70.48	-69.21
C20-C25	1.41	1.40	C8-C9-C10	118.62	118.66	N2-C3-C20-C21	-5.38	-2.25
C21-C22	1.40	1.39	C8-C9-H14	122.12	121.82	N2-C3-C20-C25	175.75	178.57
C21-H26	1.09	1.08	C10-C9-H14	119.25	119.50	C4-C3-C20-C21	-121.50	-118.54
C22-C23	1.40	1.40	C9-C10-N11	124.19	123.64	C4-C3-C20-C25	59.63	62.28
C22-H27	1.09	1.08	C9-C10-H15	119.69	120.04	H19-C3-C20-C21	113.06	116.45
C23-C24	1.41	1.40	N11-C10-H15	116.11	116.32	H19-C3-C20-C25	-65.81	-62.73
C23-C28	1.44	1.43	C10-N11-C12	116.76	117.34	C3-C4-C5-N1	6.05	5.72
C24-C25	1.39	1.38	N11-C12-C13	123.83	123.55	C3-C4-C5-N34	-175.80	-175.86
C24-H30	1.09	1.08	N11-C12-H16	116.12	116.29	C32-C4-C5-N1	-179.52	-179.07
C25-H31	1.09	1.08	C13-C12-H16	120.05	120.16	C32-C4-C5-N34	-1.37	-0.65
C28-N29	1.16	1.15	C8-C13-C12	119.01	118.73	N1-C5-N34-H35	-165.06	-167.55
C32-N33	1.17	1.16	C8-C13-H17	119.82	120.37	N1-C5-N34-H36	-21.07	-19.49
N34-H35	1.01	1.01	C12-C13-H17	121.17	120.91	C4-C5-N34-H35	16.97	14.18

Continued on next page

Table 1 continued

N34-H36	1.02	1.01	C3-C20-C21	121.63	121.83	C4-C5-N34-H36	160.96	162.25
O7-H36	1.94	1.98	C3-C20-C25	119.39	119.20	N1-C6-C8-C9	32.89	46.85
			C21-C20-C25	118.97	118.96	N1-C6-C8-C13	-151.52	-138.31
			C20-C21-C22	120.69	120.69	O7-C6-C8-C9	-146.85	-131.96
			C20-C21-H26	119.44	119.50	O7-C6-C8-C13	28.75	42.89
			C22-C21-H26	119.86	119.80	C6-C8-C9-C10	176.13	175.25
			C21-C22-C23	120.10	120.10	C6-C8-C9-H14	-2.99	-2.96
			C21-C22-H27	120.28	120.27	C13-C8-C9-C10	0.60	0.43
			C23-C22-H27	119.63	119.64	C13-C8-C9-H14	-178.52	-177.78
			C22-C23-C24	119.47	119.47	C6-C8-C13-C12	-177.68	-176.85
			C22-C23-C28	120.26	120.25	C6-C8-C13-H17	2.05	2.82
			C24-C23-C28	120.27	120.27	C9-C8-C13-C12	-1.68	-1.69
			C23-C24-C25	119.99	119.97	C9-C8-C13-H17	178.05	177.98
			C23-C24-H30	119.70	119.72	C8-C9-C10-N11	0.87	1.10
			C25-C24-H30	120.32	120.31	C8-C9-C10-H15	-179.33	-179.06
			C20-C25-C24	120.79	120.80	H14-C9-C10-N11	-179.98	179.36
			C20-C25-H31	120.21	120.26	H14-C9-C10-H15	-0.18	-0.81
			C24-C25-H31	119.00	118.94	C9-C10-N11-C12	-1.16	-1.26
			C5-N34-H35	116.19	117.06	H15-10-N11-C12	179.04	178.90
			C5-N34-H36	114.97	116.29	C10-N11-C12-C13	-0.04	-0.13
			H35-N34-H36	118.15	118.44	C10-N11-C12-H16	-179.62	-179.66
						N11-C12-C13-C8	1.47	1.61
						N11-C12-C13-H17	-178.26	-178.06
						H16-C12-C13-C8	-178.96	-178.88
						H16-C12-C13-H17	1.31	1.45
						C3-C20-C21-C22	-179.61	-179.91
						C3-C20-C21-H26	-0.19	-0.81
						C25-C20-C21-C22	-0.74	-0.73

Continued on next page

Table 1 continued

C25-C20-C21-H26	178.69	178.37
C3-C20-C25-C24	179.37	179.76
C21-C20-C25-C24	0.47	0.55
C21-C20-C25-H31	-179.87	-179.81
C20-C21-C22-C23	0.48	0.39
C20-C21-C22-H27	-179.82	-179.95
H26-C21-C22-C23	-178.95	-178.71
H26-C21-C22-H27	0.76	0.95
C21-C22-C23-C28	179.85	179.85
H27-C22-C23-C24	-179.65	-179.53
H27-C22-C23-C28	0.14	0.19
C22-C23-C24-C25	-0.33	-0.30
C22-C23-C24-H30	179.73	179.70
C28-C23-C24-C25	179.89	179.97
C23-C24-C25-H31	-179.61	-179.68
H30-C24-C25-C20	-180.00	179.96
H30-C24-C25-H31	0.34	0.32
C28-C23-C24-H30	-0.06	-0.02
C23-C24-C25-C20	0.06	-0.04
C3-C20-C25-H31	-0.97	-0.61

3.2 Vibrational Spectral Analysis of ACIDPC

ACIDPC, comprising 36 atoms, exhibits 102 normal vibrational modes, consistent with its C1 point group symmetry. Vibrational spectra were computed using DFT methods at the B3LYP/cc-PVDZ and B3LYP/cc-PVTZ levels of theory. Simulated and experimental FT-IR and FT-Raman spectra are shown in Figures 2 and 3, with detailed vibrational assignments provided in Table 2.

3.2.1. NH_2 Vibrations

The NH_2 group shows distinct symmetric and asymmetric stretching vibrations typically in the 3520–3350 cm^{-1} range, with the asymmetric stretch between 3520–3450 cm^{-1} and the symmetric stretch near 3420–3350 cm^{-1}. In this study, experimental bands were observed at 3392 cm^{-1} (asymmetric) and 3390 cm^{-1} (symmetric), closely matching the calculated values of 3415 cm^{-1} and 3412 cm^{-1}, respectively. A strong FT-IR peak at 3410 cm^{-1} further supports these assignments.

NH_2 bending modes—scissoring, rocking, wagging, and torsion—appear across a wide range: scissoring vibrations were observed at 1680 cm^{-1} (75% PED), with theoretical values at 1635 and 1631 cm^{-1}; rocking was calculated at 1203 and 1201

cm^{-1} (66% PED); wagging near 675–670 cm^{-1}; and torsional modes at 357 and 353 cm^{-1} (58% PED). These features provide insight into molecular geometry and functional group orientation.

3.2.2. N–H Vibrations

Theoretical and experimental analyses of the N–H group revealed strong agreement. Stretching modes were predicted at 3304 and 3300 cm^{-1} (98% PED) and observed experimentally at 3300 cm^{-1} [17]. In-plane bending was calculated at 1213 and 1215 cm^{-1} (72% PED), matching experimental values of 1212 cm^{-1} (FT-IR) and 1215 cm^{-1} (FT-Raman). Additional in-plane deformation modes were predicted at 1580 cm^{-1} and observed at 1582 cm^{-1} (Raman), while out-of-plane bending was predicted at 1019 and 1015 cm^{-1}, consistent with the observed 1015 cm^{-1}. This strong correlation validates the computational approach.

3.2.3. C–H Vibrations

C–H stretching vibrations typically appear in the 3100–3000 cm^{-1} range. In ACIDPC, experimental bands were detected at 3172, 3078, 3046, 2927, and 2855 cm^{-1} (FT-IR) and at 3076 cm^{-1} (FT-Raman). Theoretical predictions include peaks at 3174–2857 cm^{-1}, depending on the basis set, with PED values of 97–98%.

In-plane C–H bending modes were observed at 1551–1292 cm^{-1} (FT-IR) and 1604–1158 cm^{-1} (FT-Raman). Out-of-plane C–H bending bands appeared at 1154–872 cm^{-1} (FT-IR) and 1094–931 cm^{-1} (FT-Raman), with theoretical matches between 1002–745 cm^{-1}, supporting the accuracy of the computed spectra.

3.2.4. C–C Vibrations

C–C stretching vibrations in aromatic systems typically occur between 1650 and 1400 cm^{-1}. Experimental peaks were recorded at 1607, 1602, 1575, 1554, 1439, and 1418 cm^{-1}, among others. Theoretical values closely matched these, with major bands predicted at 1604–1137 cm^{-1} and PED contributions of 68–69%. FT-Raman peaks at 1580 and 1582 cm^{-1} further support the assignments.

Table 2. Vibrational assignments, observed and calculated wavenumbers (scaled) of 5-Amino-3-(4-cyanophenyl)-1-isonicotinoyl-2,3-dihydro-1*H*-pyrazole-4-carbonitrile at B3LYP method with B3LYP/cc-pVDZ and B3LYP/cc-pVTZ basis set

Mode no	Observed Wavenumbers (cm^{-1})		Calculated wavenumbers (cm^{-1})		Vibrational Assignments (PED %)
	FT-IR	FT-Raman	B3LYP / cc-pvDZ	B3LYP / cc-pvTZ	
$\nu 1$	3410		3415	3412	$\upsilon_{ass}NH_2$(99)
$\nu 2$	3356		3361	3355	$\upsilon_{ss}NH_2$(98)
$\nu 3$	3300		3304	3300	υNH(98)
$\nu 4$	3172		3174	3171	υCH(98)
$\nu 5$			3115	3112	υCH(98)
$\nu 6$			3088	3085	υCH(98)
$\nu 7$	3078	3076	3079	3077	υCH(98)
$\nu 8$			3059	3058	υCH(98)
$\nu 9$	3046		3048	3045	υCH(97)
$\nu 10$			2990	2987	υCH(97)
$\nu 11$	2927		2931	2928	υCH(98)
$\nu 12$	2855		2860	2857	υCH(97)
$\nu 13$	2227	2230	2234	2232	υCN(92)
$\nu 14$			1680	1677	υCN(92)
$\nu 15$	1680		1676	1670	υCO(72), $_{siccsoring}NH_2$(18)
$\nu 16$			1635	1631	$_{siccsoring}NH_2$(75), υCN(18)
$\nu 17$		1604	1607	1604	υCC(68);CH(22);
$\nu 18$			1602	1598	υCC(66); $_{siccsoring}NH_2$ (17)
$\nu 19$	1580	1582	1592	1590	NH(68); υCC(20)
$\nu 20$			1575	1572	υCC(68);CH(22)
$\nu 21$	1551	1553	1554	1550	υCC(66);CH(22)
$\nu 22$			1534	1531	CH(72)

Continued on next page

Table 2 continued

ν23	1500		1506	1503	CH(72)
ν24	1460		1468	1461	CH(73)
ν25			1455	1450	υCN(75) CH(17);
ν26			1439	1437	CH(76);υCC(10)
ν27	1413	1415	1418	1415	CH(75);υCC(12)
ν28	1367	1369	1375	1370	CH(76)
ν29			1346	1343	CH(70); υCN(13); CO(10)
ν30			1320	1321	CH(72); υCN(12)
ν31	1292	1294	1298	1294	CH(74)
ν32			1276	1275	υCC(69); CC(74)
ν33			1252	1251	υCC(68); CH(16)
ν34			1240	1237	υCC(70)
ν35	1212	1215	1215	1213	NH(72)
ν36			1203	1201	σ rockingNH_2(66); υCC(10)
ν37			1194	1192	υCC(69)
ν38			1180	1181	υCC(68)
ν39			1174	1170	υCC(68)
ν40	1156	1158	1158	1157	CH(64); υCC(18); υCN(10)
ν41			1140	1137	υCC(68)
ν42			1130	1129	CC(66)
ν43	1111		1115	1112	υNN(68)
ν44			1090	1089	CC(66)
ν45	1061		1064	1060	υCN(68)
ν46			1035	1033	υCN(68); NH(18)
ν47	1015		1019	1015	γNH(61)
ν48			1007	1004	$_{CH}$(60)
ν49			1002	997	γCH(60)
ν50			990	988	γCH(60)
ν51	971		974	970	γCH(61)
ν52			955	953	$_{ring}$(71)
ν53	933		943	942	υCN(66); CO(17)
ν54			933	931	CO(62); σ rocking(15)
ν55			910	907	γCH(61)
ν56			866	865	γCH(60)
ν57	832		834	830	γCH(61)
ν58			812	810	γCH(60)
ν59			800	794	υCN(62); CH(14)
ν60	786	787	781	786	CN(63)
ν61			764	761	υCC(62); CN(12)
ν62	743		746	745	γCC(60); γCH(12)
ν63	721		720	720	$_{ring}$(61)
ν64			710	707	$_{ring}$(64)
ν65			695	693	γCO(61)
ν66	688		691	688	γCN(54)
ν67			675	670	$\gamma_{waggingNH2}$(64)
ν68			660	657	CC(62)
ν69			644	641	$_{ring}$(61)
ν70	619	619	625	620	$_{ring}$(59)
ν71			606	602	γCC(58)
ν72			575	572	γCC (58)
ν73	552		560	556	$_{ring}$(60)
ν74			551	548	CC(60)
ν75			540	537	$_{ring}$(61)
ν76			525	521	CCC(60)
ν77			505	502	$_{ring}$(60)

Continued on next page

Table 2 continued

ν78	464	463	γ_{ring}(52)
ν79	456	452	γ CC(51)
ν80	451	448	CCC(63)
ν81	426	424	$_{ring}$(61)
ν82	405	401	$_{ring}$(62)
ν83	402	399	γ_{ring}(58)
ν84	380	378	γ_{ring}(51)
ν85	357	353	τ NH_2 (58)
ν86	299	297	$_{ring}$(60)
ν87	280	276	$_{ring}$(62)
ν88	270	269	$_{ring}$(62)
ν89	245	240	CC(65)
ν90	216	212	γ_{ring}(51)
ν91	204	201	γ_{ring}(50)
ν93	164	159	γCC(49)
ν93	125	123	γCN(51)
ν94	111	108	γ_{ring}(52)
ν95	95	93	γCC(50)
ν96	80	76	τ CC(49)
ν97	66	65	τ CC(49)
ν98	57	53	γ_{ring}(52)
ν99	44	40	γ_{ring}(50)
100	30	26	γ_{ring}(50)
101	25	22	γCC(50)
102	14	12	γ_{ring}(51)

υ; Stretching, $\upsilon_{ass;}$ asymmetric Stretching, $\upsilon_{ss;}$ symmetric Stretching, δ; in-plane bending, γ; out-of-plane bending, τ; torsion

3.2.5. C=O Vibrations

Carbonyl (C=O) stretching typically occurs between 1870 and 1550 cm^{-1}. ACIDPC exhibits a strong FT-IR band at 1680 cm^{-1}, with calculated values at 1676 and 1670 cm^{-1} (72% PED). Deformation vibrations were predicted at 933 and 931 cm^{-1}, matching the experimental value of 933 cm^{-1}. Bending vibrations at 695 and 693 cm^{-1} also align with theoretical results. These findings are consistent with literature data [18].

3.2.6. C = N and C–N Vibrations

C = N stretching is typically found between 2400 and 2200 cm^{-1}. A strong FT-IR band at 2227 cm^{-1} was observed, with VEDA analysis indicating a 92% C = N stretching contribution. The C=N stretch in the pyrazole ring appears at 1677 cm^{-1}.

C–N stretches often overlap with other bands in the 1400–1200 cm^{-1} region. Experimental bands were found at 1455, 1064, and 943 cm^{-1}, corresponding to theoretical predictions at 1450, 1060, and 942 cm^{-1}, with PED values of 75%, 68%, and 66%, respectively. Slight shifts are attributed to interactions with C–C modes. The close agreement between calculated and experimental values confirms the accuracy of these assignments.

3.3 Molecular electrostatic potential (MEP) surface analysis

Molecular Electrostatic Potential (MEP) calculations are critical for identifying charge distribution and highlighting reactive sites within a molecule. This method is particularly useful for pinpointing electrophilic and nucleophilic regions, as well as sites prone to hydrogen bonding interactions [18]. Using GaussView 5.0 software [11], a 3D color-coded map (**Supplementary Fig. S1**) was generated to visualize the molecular electrostatic potential. In the ACIDPC molecule, the nitrogen atoms in the pyrazole ring exhibit electron-rich properties, resulting in a negative electrostatic potential. These electronegative nitrogen atoms withdraw electron density from adjacent carbon atoms, creating regions of positive electrostatic potential around the carbons. Additionally, the red-colored nucleophilic region surrounding the nitrile group (-C28 = N29) and the carbonyl group (C6=O7) represents the most electronegative areas, indicating favorable sites for electrophilic attacks. Such spatial polarity and charge delocalization distinguish it from previous pyrazole analog [15] enhancing its binding affinity and reactivity.

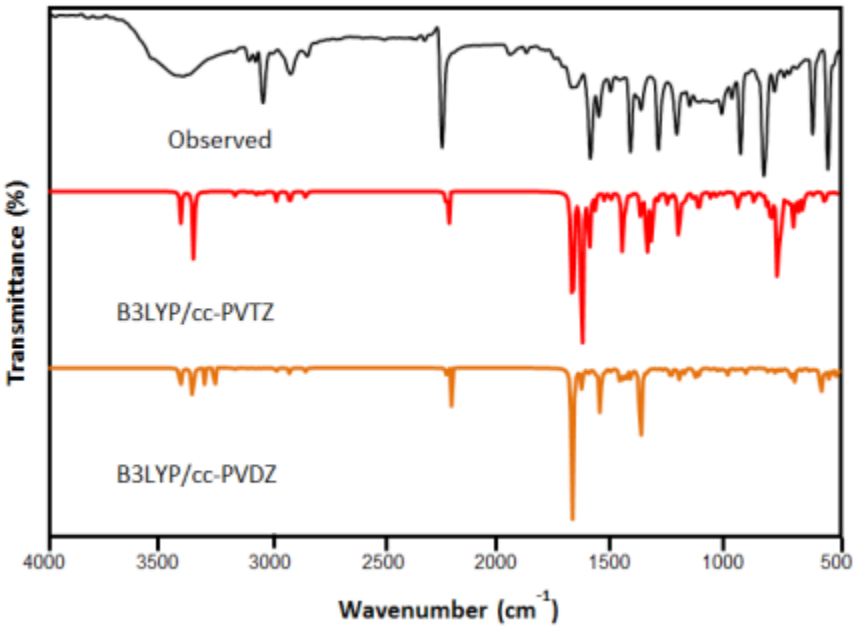

Fig 2. Experimental and calculated FT-IR spectra 5-Amino-3-(4-cyanophenyl)-1-isonicotinoyl-2,3-dihydro-1H-pyrazole-4-carbonitrile

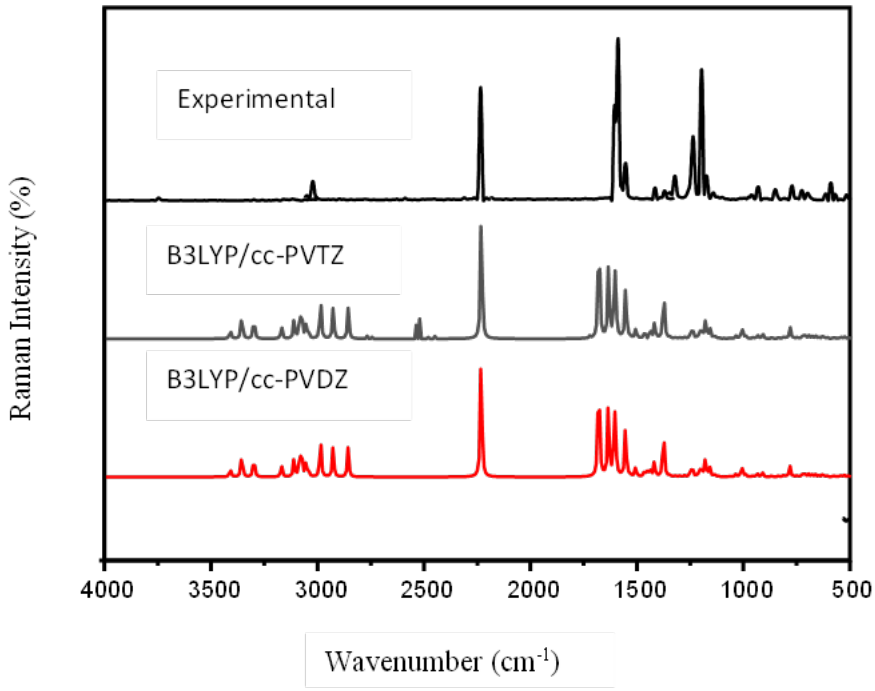

Fig 3. Experimental and calculated Raman spectra of 5-Amino-3-(4-cyanophenyl)-1-isonicotinoyl-2,3-dihydro-1H-pyrazole-4-carbonitril

3.4 Molecular stabilisation analysis

A significant advantage of Natural Bond Orbital (NBO) analysis is its ability to precisely examine intramolecular bonding and the interactions between various bonds. The high value of E(2) indicates a strong tendency for electron donors and acceptors to exchange electrons, suggesting enhanced interaction and greater conjugation within the system [19]. Stabilizing donor-acceptor interactions occur when electron density is shared between occupied Lewis-type NBO orbitals (e.g., bonds or lone pairs) and formally unoccupied non-Lewis NBO orbitals (such as antibond or Rydberg orbitals). Second-order perturbation theory is used to quantify the energy associated with these interactions, offering a detailed description of intramolecular interactions. According to NBO analysis (**Supplementary Table S1**), the strongest stabilization interaction occurs between LP(1) N33 $\rightarrow\pi^{\star}$ (C4–C5) with 55.89 kcal/mol. Notable contributions also include π (C20–C21) $\rightarrow\pi^{\star}$ (C24–C25) (20.75 kcal/mol) and π (C22–C23) (21.55 kcal/mol). The lone pair on N1 stabilizes $\pi^{\star}$ (C6–C7) (49.66 kcal/mol) and $\pi^{\star}$ (C4–C5) (35.62 kcal/mol), while LP(2) O7 $\rightarrow\sigma^{\star}$ (N1–C6) provides 23.15 kcal/mol. For comparison, halogen-substituted pyrazole derivative [18], reflecting weaker charge delocalization, presumably because of the lack of strong electron-withdrawing groups or extended conjugation in those molecules. A primary distinguishing aspect in ACIDPC is that it contains two or more electron-rich (pyrazole N, amino) and electron-poor (nitrile, pyridine N, carbonyl) sites in one conjugated heterocyclic molecule that enables wider resonance stabilization as well as broader intramolecular charge transfer over relatively simple ones. The coexistence of nitrile functional group (C = N) beside the pyrazole also helps in efficient charge migration that does not widely appear in the earlier literature.

3.5 Analysis of structure-activity descriptor

3.5.1. Fukui Indices

The Fukui function is calculated using specific relationships to assess the reactivity of the molecule. The electron populations for atoms in their neutral, cationic, and anionic states within a system are denoted as $q_r(N)$, $q_r(N-1)$,$q_r(N+1)$, respectively. The reactivity parameters, denoted as $f^{-}(\vec{r})$, $f^{+}(\vec{r})$ are linked to electrophilic and nucleophilic attacks, respectively. The dual descriptor $\Delta f(r) = f^{+}(\vec{r}) - f^{-}(\vec{r})$ allows for the identification of sites within a system where electrophilic attacks (f(r) < 0) and nucleophilic attacks (f(r) > 0) are favoured simultaneously at point r. Based on the calculations in (**Supplementary Table S2**), atoms such as C6, C5, H35, H36, H18, C28, H17, H14, H16, H15, H19, H31, H30, H27, H26, C10, and C12, which exhibit negative dual descriptor values (f(r)), are more prone to electrophilic attacks. Conversely, atoms like N34, N2, O7, N1, N29, C21, N11, C25, C22, C23, C24, C13, C9, and N33, with positive f(r) values, are more susceptible to nucleophilic attacks. These reactive sites align well with those identified in the Molecular Electrostatic Potential (MEP) analysis, reinforcing the reliability of the Fukui function in predicting molecular reactivity.

3.5.2. Frontier molecular orbital (FMO) analysis

The role of Frontier Molecular Orbitals (FMOs) in biological reactivity has garnered significant attention, particularly due to their correlations with properties such as antimicrobial, anticancer [20], antifungal, and cytotoxic activities. This has paved the way for new opportunities in drug design. The energy levels and energy gap of FMOs (E_{HOMO}, E_{LUMO}, and ΔE) provide key insights into parameters like ionization potential ($I = -E_{HOMO)}$ and electron affinity ($A = -E_{LUMO.}$ Moreover, FMOs are instrumental in assessing various chemical reactivity descriptors, calculated using the following equations: Ionization Potential ($I = -E_{HOMO}$; Electron Affinity ($A = -E_{LUMO}$; Chemical Potential (ϕ) = −(I + A)/2; Absolute Hardness (η) = (I − A)/2; Softness (S) = $1/\eta$; Electronegativity (χ) = (I + A)/2; Electrophilicity Index (ω) = $\phi^2/2\eta$.

The HOMO value of the compound is −6.28 eV, the LUMO is −2.18 eV, and the energy gap (ΔE) is 4.10 eV, as shown in **Supplementary Fig. S2**. The electronegativity ($\chi = -4.23$eV) reflects the molecule's ability to accept electrons, representing its Lewis acidity. The global hardness (η = 2.05 eV) indicates the molecule's resistance to charge transfer, while global softness (S = −0.49 eV) represents the molecule's electron transport capacity. Soft compounds, with smaller FMO energy gaps (ΔE = 4.10 eV), are more reactive in electron transfer compared to harder compounds. The electrophilicity index (ω = −4.38 eV) quantifies the molecule's ability to attract an additional electron and resist electron exchange with its environment. Zeyrek CT et al. [15] reported energy gap value 4.23 eV for 3-(4-chlorophenyl)-5-(4-ethoxyphenyl)-4,5-dihydropyrazole-1-carbonitrile, which lacks the electron-rich pyridine and amino substituents present in ACIDPC. In comparison, the energy gap observed for ACIDPC reflects a unique balance between conjugation and the polarity of functional groups, resulting in an intermediate band gap that facilitates both electronic delocalization and site-specific interactions. This characteristic is conducive to intramolecular charge transfer (ICT), as indicated by the orbital distribution maps (**Supplementary Fig. S2**).

3.6 Electronic absorption spectrum

The computational electronic absorption spectrum, obtained using TD–DFT/B3LYP/cc-pVTZ, is summarized in Table 3, with major molecular orbital contributions calculated using the Gaussian 2.2 program[21]. The absorption spectra shown in **Supplementary Fig. S3** indicate that the first excited states result from electron transfer from the HOMO to the LUMO. The close proximity of the HOMO and LUMO energy levels suggests that the electronic absorption is linked to intramolecular charge transfer. This involves excitation from donor groups in the HOMO to acceptor groups in the LUMO through a conjugated pathway. Experimentally, absorption peaks were observed at 303 nm, 297 nm, and 224 nm, with corresponding excitation energies of 2.17 eV, 2.12 eV, and 3.98 eV, respectively, in the gas phase.

Table 3. Theoretical electronic absorption spectra of 5-Amino-3-(4-cyanophenyl)-1-isonicotinoyl-2,3-dihydro-1H-pyrazole-4-carbonitrile (absorption wavelength λ (nm), excitation energies, E (eV) and oscillator strengths (f) using TD–DFT/B3LYP/cc-pVTZ methods in gas phase

Solvent	E (ev))	λ(nm)	f	[a]Major contribution
Gas	3.64	340.06	0.1073	HOMO->LUMO (98%)
	4.03	307.3	0.0205	HOMO->L+1 (99%)
	4.24	291.96	0.0016	H-2->LUMO (90%)
Methanol	2.95	338.16	0.1368	HOMO->LUMO (98%)
	3.11	321.35	0.0178	HOMO->L+1 (99%)
	3.51	284.74	0.0022	H-3->LUMO (29%), H-2->LUMO (31%), H-1->LUMO (34%)

[a] H – HOMO, L – LUMO.

3.7 Non-Covalent Interactions (NCI)

The electron density, ρ(r), is initially calculated to establish the reduced density gradient (RDG), a key non-dimensional variable used in analyzing weak interactions. This highly effective technique, for understanding intermolecular interactions[22]. The RDG expression is given by:

$$RDG(r) = \frac{1}{2(3\pi)^{\frac{1}{3}}} \frac{|\Delta\rho(r)|}{\rho(r)^{\frac{4}{3}}}$$

Multiwfn 3.7 and VMD 1.9.3 were employed to generate RDG plots for the title compound, as shown in **Supplementary Fig. S4**, aiding in the visualization of intermolecular interactions[23]. RDG spikes, $\lambda 2$ values, and RDG clusters serve as indicators of bond types and interaction strength in RDG analysis. In this context, Van der Waals interactions exhibit values near zero ($\rho \approx 0$, $\lambda 2 \approx 0$), while hydrogen interactions show large negative $\lambda 2$ values, corresponding to high density values ($\rho > 0$, $\lambda 2 < 0$), which indicate strong repulsive interactions[22]. **Supplementary Fig. S5** highlights various interactions using color coding: red indicates steric repulsion between the pyridine, pyrazole, and nitrobenzene rings, blue represents strong hydrogen bonds, and green denotes Van der Waals interactions. RDG plot analysis reveals that Van der Waals interactions dominate in the molecule, emphasizing their significance in the chemical system.

3.8 Localized orbital locator (LOL) and electron localization function (ELF)

The 2D representation of the ELF isosurface for the pyrazole derivative, generated using the Multiwfn 3.7 program[23], is shown in Figure 4a. This figure highlights electron localization through orange and red regions, while depletion zones between the inner and valence shells are indicated by blue circles[24]. Specifically, the hydrogen atoms H14 and H19 exhibit highly localized electron density, suggesting strong bonding interactions, while the blue regions surrounding carbon (C8, C9, C10, C12, C13) and nitrogen atoms (N2, N11) point to a delocalized electron cloud. This delocalization is indicative of a stable electronic structure that may influence the compound's reactivity. Furthermore, Figure 4b illustrates a white central region around a hydrogen atom, indicating electron density exceeding the upper limit of the color scale. These findings suggest that the pyrazole derivative possesses a complex electron distribution, which may play a crucial role in its chemical behaviour and potential reactivity. The analysis of this study demonstrates ELF and LOL assessments for the first time on a pyrazole–pyridine hybrid compound with nitrile and isonicotinoyl binding groups. The combined assessment through these methods establishes strong conjugation, electronic coherence and enhances our understanding of the stability of the molecule while showing improved charge transfer competence that underpins its drug-receptor binding and optical responsiveness. By applying

combined topological analysis, the understanding of reactivity mechanisms grows stronger while providing essential knowledge for future development of heterocyclic pharmacophores.

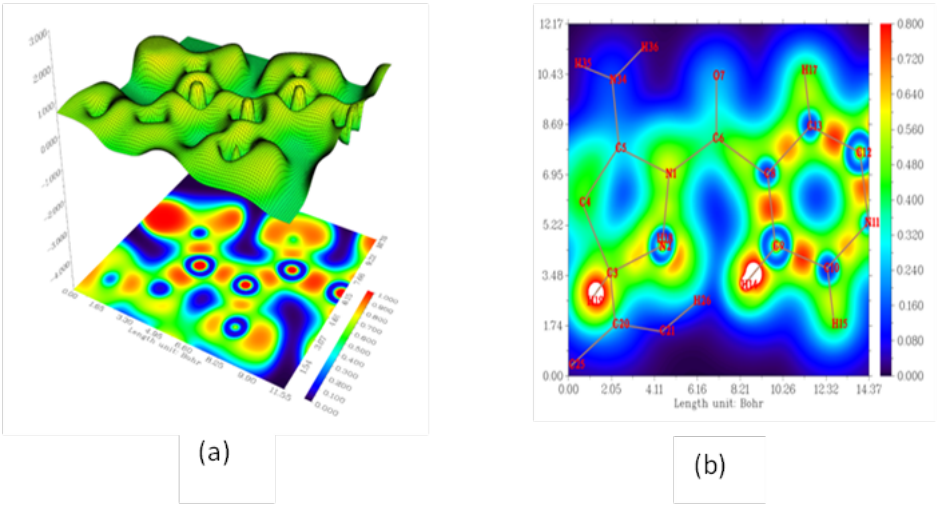

Fig 4. (a) ELF color-filled map of ACIDPC and (b) LOL color-filled map of 5-Amino-3-(4-cyanophenyl)-1-isonicotinoyl-2,3-dihydro-1H-pyrazole-4-carbonitrile

3.9 A BOILED-Egg Model for Predicting Gastrointestinal Absorption and Brain Penetration of Small Molecules

The BOILED-Egg approach, utilizing the SMILES string of chemical compounds, predicts gastrointestinal (GI) absorption and blood–brain barrier (BBB) permeability. The algorithm considers two key physicochemical factors: polarity, represented by the topological polar surface area (TPSA), and lipophilicity, measured by WLOGP. The model was refined using data from compounds with known varying gastrointestinal (GI) absorption and blood-brain barrier (BBB) penetration properties. As shown in **Supplementary Fig. S6**, the compound in question falls within the yellow zone, signifying strong absorption and efficient penetration across both the GI tract and BBB. In contrast, compounds positioned in the whitish region exhibit strong GI absorption but poor BBB penetration. The model also accounts for potential efflux from the central nervous system (CNS) via P-glycoprotein (PGP), with blue (+) and red (—) dots indicating compounds that are either substrates or inhibitors of PGP. For ACIDPC, the red dot's position indicates high GI absorption but limited BBB penetration, suggesting it is a promising therapeutic candidate with favorable transport properties for systemic administration.

3.10 Molecular docking studies

The optimized protein structures were employed in molecular docking studies using AutoDock Tools (ADT)[14],[15]. Figure 5. illustrates the protein-ligand complex, depicting the interactions between the ligand, ACIDPC, and the target proteins associated with insulin inhibition, antimicrobial activity, and antineoplastic properties. The Ramachandran plot in **Supplementary Fig. S7** was used to evaluate the quality of the protein structures. The molecular docking analysis involved docking the ligand ACIDPC at the functional sites of the selected proteins, determining the minimum docking energy values. The interactions between ACIDPC and the target proteins were analyzed, revealing specific binding modes and potential inhibitory properties. Upon successful docking, the analysis provided data on binding energies and inhibition constants, as summarized in Table 4, along with the minimum docking energy values.

For the protein 2CI2, the active site interacted with the ACIDPC compound, with residues such as VAL I:57 (3.46 Å) forming a conventional hydrogen bond with the nitrogen in the pyridine group. Other interactions included ARG I:81 (4.57 Å), PHE I:69 (5.17 Å), and LEU I:68 (4.09 Å), which exhibited π-cation, π-π alkyl, and carbon-hydrogen bonds with different parts of the ligand. In the case of 2EA9, residues such as GLY A:55 (3.76 Å), PHE A:52 (5.98 Å & 5.00 Å), and SER A:16 (3.49 Å) formed conventional hydrogen bonds with the pyridine and pyrazole rings of the compound, while SER A:19 (3.59 Å) participated in a carbon-hydrogen bond interaction. For the antineoplastic protein 6KLK, GLN A:100 (5.73 Å) and ASN A:97

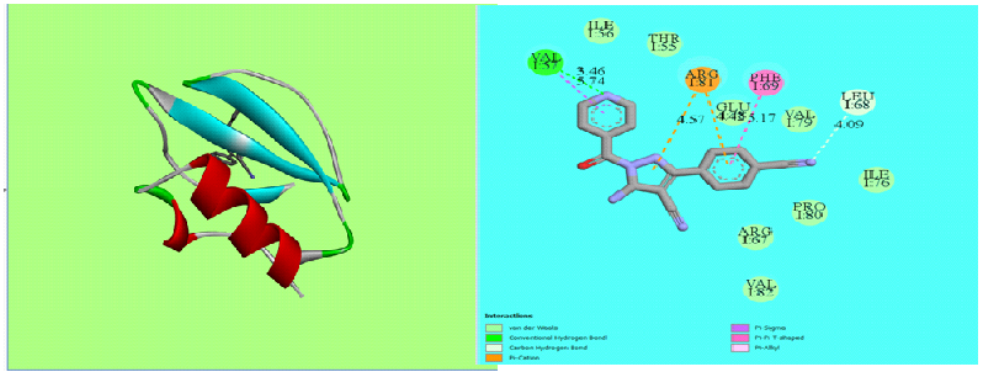

(a)

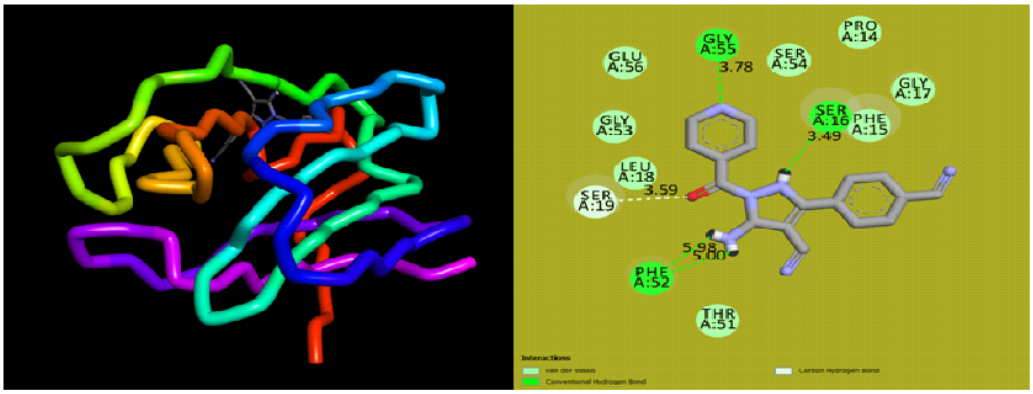

(b)

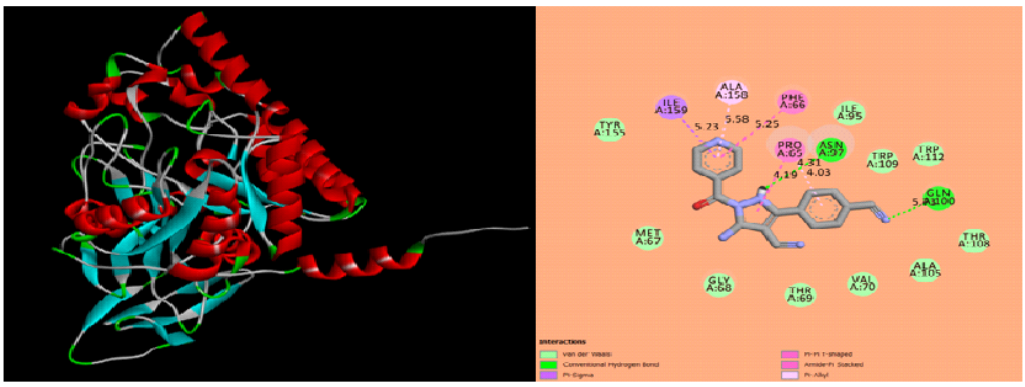

(c)

Fig 5. Schematic diagram for the docked confirmation of the active site of the title compound with, (a) 2CI2 (Insulin Inhibitor), (b)2EA9 (Antimicrobial), (c) 6KLK (antineoplastic protein)

(4.31 Å) interacted with the carbonitrile and pyrazole groups of the ligand. Additionally, residues such as ILE A:159 (5.23 Å), ALA A:158 (5.58 Å), PHE A:66 (5.25 Å), and PRO A:65 (4.19 Å) exhibited pi-sigma, π-alkyl, and π-π alkyl interactions with the pyridine and carbonitrile groups of the ligand.

Table 4. Bond distance between ligand and residues

Ligand	**Protein PDB ID (2CI2)**	
ACIDPC	**Residues**	**Bond distance(Å)**
	ARG I:81	4.57
	VAL I:57	3.46
	PHE I:69	5.17
	LEU I:68	4.09
Estimated Inhibition Constant (μm): 12.93		
Binding Energy (kcal/mol): -6.67		
RMSD: 14.06		
Ligand	**Protein PDB ID (2EA9)**	
ACIDPC	**Residues**	**Bond distance(Å)**
	GLY A:55	3.78
	SER A:16	3.49
	PHE A:52	5
	SER A:19	3.59
	PHE A:52	5.98
Estimated Inhibition Constant (μm): 4.24		
Binding Energy (kcal/mol): -7.33		
RMSD: 21.97		
Ligand	**Protein PDB ID (6KLK)**	
ACIDPC	**Residues**	**Bond distance(Å)**
	ILE A:159	5.23
	AAL A:158	5.58
	PHE A:66	5.25
	PROA:65	4.19
	ASN A:97	4.31
	GLN A:100	5.73
Estimated Inhibition Constant (μm): 2.13		
Binding Energy (kcal/mol): -7.74		
RMSD: 46.15		

The binding energies (kcal/mol) and inhibition constants (μM) for the interactions with 2CI2, 2EA9, and 6KLK are provided in Table 4. The bioactive nature of the molecule was demonstrated by the lowest binding energy value. Among the protein receptors, 6KLK exhibited the lowest binding energy of -7.74 kcal/mol, indicating a strong interaction with the ligand. This receptor, containing six residues, formed hydrogen bonds with lengths of 4.31 Å and 5.73 Å. ACIDPC was found to interact with multiple receptors, with the antineoplastic protein 6KLK showing the most favorable interaction, as highlighted in Figure 5.

3.11 Antimicrobial activity

The *in-vitro* antibacterial activity of the ACIDPC compound was evaluated using the agar well diffusion method. In this approach, a 100 μL well was aseptically created on the agar plate surface, followed by inoculation with bacterial strains. Various concentrations of the ACIDPC sample were then added to the wells, and the plates were incubated under suitable conditions. The antimicrobial component diffused through the agar medium, inhibiting the growth of the tested bacterial strains. The antibacterial activity was determined by measuring the diameter of the inhibitory zones surrounding each well. In this study, ACIDPC was tested at four concentrations (25 μL, 50 μL, 75 μL, and 100 μL) against both gram-negative *Escherichia coli* (*E. coli*) and gram-positive *Staphylococcus aureus* (*S. aureus*) strains. *E. coli* is associated with various infections, including urinary

tract infections, pneumonia, pelvic infections, and meningitis, while *S. aureus* is known to cause skin infections, endocarditis, and bloodstream infections.

After 24 hours of incubation at 37°C, inhibitory zone diameters were measured (**Supplementary Table S3**), revealing a clear correlation between increasing ACIDPC concentrations and enhanced antibacterial activity against *E. coli* and *S. aureus* (**Supplementary Figs. S8 and S9**). ACIDPC exhibited significant inhibition, with zones of 20 mm for *E. coli* and 18 mm for *S. aureus*, suggesting strong antibacterial efficacy. This activity is likely due to the carbonitrile group in the pyrazole ring, which may disrupt bacterial cellular processes. These findings position ACIDPC as a promising candidate for antimicrobial development.

3.12 Drug likeness evaluation and ADME/Tox Properties

The drug-like properties of ACIDPC were evaluated based on its physicochemical attributes and ADMET (absorption, distribution, metabolism, excretion, and toxicity) characteristics[22] using the ADMETlab 3.0 online server (Table 5). This pharmacokinetic assessment aimed to predict ACIDPC's safety and oral bioavailability, which are critical for regulatory approval. Lipinski's Rule of Five was applied to assess its suitability for oral administration. Given the importance of ADMET profiling in drug discovery, further experimental validation is needed to confirm its pharmacokinetic behavior and toxicity profile. According to Lipinski's Rule of Five, a drug-like molecule should have a molecular weight under 500 Daltons, a surface area under 140 $Å^2$, fewer than five hydrogen bond donors, a logP value under 5, and fewer than 10 rotatable bonds. The bioavailability and toxicity radar charts for ACIDPC are depicted in **Supplementary Figs. S10 and S11**. ACIDPC has a molecular weight of 316.11 Daltons. It has seven hydrogen bond acceptors and three hydrogen bond donors, making it a strong candidate for drug development due to its compliance with all five Lipinski rules.

Table 5. ADME properties of ACIDPC

Entry	ABS	TPSA (A^2)	n-ROTB	MW	LogP	n-OHN acceptors	n-OHNH donors	Lipinski's violations	Veber Violations	Egan Violation	S.A
				<500	<=5	<10	<5	<=1	<=1	<=1	0 <S.<10
ACIDPC	High	118.83	3	316.11	0.35	7	3	0	1	1	3.74

Abbreviations: ABS: Absorption, TPSA: Topological Polar Surface Area, n-ROTB: Number of Rotatable Bonds, MW: Molecular Weight, Log P: logarithm of partition coefficient of compound between n-octanol and water, n-ONHN acceptors: Number of hydrogen bond acceptors, n-OHNH donors: Number of hydrogen bonds donors, S.A: Synthetic accessibility.

A comprehensive analysis of ACIDPC's ADMET and physicochemical properties is presented in (**Supplementary Table S4**). Using the ADMET Lab 3.0 web server, the evaluation provides precise, quantitative insights into ACIDPC's drug-like characteristics. Key physicochemical parameters, such as logS (-4.854), logD, and logP, were determined, reflecting a strong focus on optimizing solubility and distribution profiles. Absorption parameters, including CaCO2 permeability (-4.854), P-gp inhibitor/substrate (P-gp) at 0.033, and human intestinal absorption (HIA) at 0.017, support the compound's efficient absorption through the small intestine. The bioavailability values at 20% (F20%) and 30% (F30%) further emphasize this potential. Distribution factors, including plasma protein binding (PPB) and volume of distribution (VD), were quantified, as well as excretion properties such as half-life (T1/2) and clearance (Cl). These favorable predictions across various parameters not only demonstrate ACIDPC's potential as a promising drug candidate but also highlight the role of precision and innovation in advancing therapeutic research. The pharmacokinetic evaluation in the study was conducted entirely through in silico methods. Using, computational tools such as SwissADME and ADMETlab3.0 (Adsorption, Distribution, Metabolism, Excretion and Toxicity) parameters. SwissADME was used to assess properties like oral bioavailability, gastrointestinal absorption, blood-brain barrier permeability, and P-glycoprotein interaction. ADMATlab3.0 was utilized to predict parameters including volume of distribution, total clearance, renal and hepatic toxicity, and potential drug-drug interactions. These tools allowed us to gain preliminary insights into the pharmacokinetic behaviour of the compounds. Therefore, ACIDPC can be a better drug candidate for antimicrobial activity, after investigated through in vitro approaches.

3.13 Physiochemical and Medicinal chemistry properties

While the ligand exhibits promising physicochemical and medicinal chemistry properties, it does not fully meet the rigorous criteria required for classification as a potent drug candidate. As shown in **Supplementary Tables S5 and S6 and Supplementary Fig. S12**, key bioavailability and drug-like parameters have been systematically evaluated. The

bioavailability radar provides critical insights into the compound's pharmacokinetic suitability, revealing areas that require further optimization. The novelty of this research lies in its comprehensive assessment of the ligand's potential using advanced in silico tools, which offer precise predictions of bioavailability and drug-likeness. Unlike conventional screening methods, this approach integrates multiple predictive models to identify key limitations early in the drug development pipeline. Future studies should focus on refining these properties through structural modifications and experimental validation, ensuring an optimal balance between efficacy, bioavailability, and safety.

4 Conclusion

The vibrational spectral analysis and quantum chemical calculations of 5-Amino-3-(4-cyanophenyl)-1-isonicotinoyl-2,3-dihydro-1H-pyrazole-4-carbonitrile (ACIDPC) reveal key molecular interactions, particularly the stabilization from lone pairs on N33 and N1 interacting with π^* orbitals in the C4-C5 and C6-C7 regions. The calculated dipole moment of 6.15 Debye indicates strong binding affinity and potential for significant biological activity. In contrast to earlier studies that predominantly examined pyrazole derivatives with limited functional diversity and single-target activity, ACIDPC features a diverse array of pharmacophoric groups—including amino, nitrile, cyanophenyl, carbonyl, and isonicotinoyl units—integrated into a single molecular framework. This design leads to improved electron delocalization, site-specific reactivity, and multi-target bioactivity. When compared to previous research which focused on pyrazole analogues with fewer conjugated systems and lower bioactivity scores, AClIDPC exhibits higher donor–acceptor stabilization energies (up to 55.89 kcal/mol), a balanced HOMO–LUMO energy gap of 4.10 eV. The bioavailability score of 0.55 and favorable ADMET properties suggest ACIDPC's promising pharmacological potential, with good absorption, distribution, and safety profiles. Molecular docking studies with proteins (PDB IDs: 2CI2, 2EA9, 6KLK) showed stable binding affinities of -6.67, -7.33, and -7.74 kcal/mol, indicating potential as an antineoplastic drug. Additionally, ELF and LOL analyses suggest a more extensive electron delocalization relative to similar systems reported previously, indicating enhanced charge transfer capabilities and the compound exhibited strong antibacterial activity against *E. coli* and *S. aureus*. The incorporation of in silico ADMET and BOILED-Egg analysis further supports the compound's favorable pharmacokinetic and safety profiles—an aspect often overlooked in prior studies. The identification of dual activity (antimicrobial and anticancer) within a single compound, along with its structural, electronic, and bioactivity advantages, distinguishes this study from existing literature and lays a solid foundation for future drug development and optimization.

References

1) Moussa Z, Ramanathan M, Alharmoozi SM, Alkaabi SAS, Aryani SHMA, Ahmed SA, et al. Recent highlights in the synthesis and biological significance of pyrazole derivatives. *Heliyon*. 2024 Oct;10(20):e38894. https://doi.org/10.1016/j.heliyon.2024.e38894.
2) Adardour M, Lahcen MA, Oubahmane M, Ettahiri W, Hdoufane I, Bouamama H, et al. Design, synthesis, molecular modeling and biological evaluation of novel pyrazole benzimidazolone derivatives as potent antioxidants. *Pharmaceuticals*. 2023;16(12):1648. https://doi.org/10.3390/ph16121648.
3) Ali AAS, Khan D, Naqvi A, Al-Blewi FF, Rezki N, Aouad MR, et al. Design, synthesis, molecular modeling, anticancer studies, and density functional theory calculations of 4-(1,2,4-triazol-3-ylsulfanylmethyl)-1,2,3-triazole derivatives. *ACS Omega*. 2021;6:301–316. https://doi.org/10.1021/acsomega.0c04595.
4) Lusardi M, Spallarossa A, Brullo C. Amino-pyrazoles in medicinal chemistry: A review. *Int J Mol Sci*. 2023;24(9):7834. https://doi.org/10.3390/ijms24097834.
5) Bavishi A, Vala H, Swami S, Thakrar S, Shah A, Sarkar D. Regio selective synthesis of pyrazole derivatives of 5-chloro-2-methoxy phenyl hydrazide and their biological evaluation. *J Heterocycl Chem*. In Press, Corrected Proof. https://doi.org/10.1002/jhet.4941.
6) Abouelenein MG, Ismail AEAH, Aboelnaga A, Tantawy MA, El-Ebiary NMA, El-Assaly SA. Synthesis, DFT calculations, in silico studies, and biological evaluation of pyrano[2,3-c]pyrazole and pyrazolo[4',3':5,6]pyrano[2,3-d]pyrimidine derivatives. *Mol Struct*. 2023 Nov;1291:136023. https://doi.org/10.1016/j.molstruc.2022.134587.
7) Takić M, Ranković S, Girek Z, Pavlović S, Jovanović P, Jovanović V, et al. Current insights into the effects of dietary α-linolenic acid focusing on alterations of polyunsaturated fatty acid profiles in metabolic syndrome. *Int J Mol Sci*. 2024;25(9):4909. https://doi.org/10.3390/ijms25094909.
8) Turkan F, Cetin A, Taslimi P, Karaman M, Gulçin İ. Synthesis, biological evaluation and molecular docking of novel pyrazole derivatives as potent carbonic anhydrase and acetylcholinesterase inhibitors. *Bioorg Chem*. 2019;86:420–427. https://doi.org/10.1016/j.bioorg.2019.02.013.
9) Niranjana SV, Lokanath NK. Synthesis, structural analysis, theoretical calculations, and pharmaceutical evaluation of a novel pyrazole derivative: Investigating the impact of lattice solvents on its properties. *J Mol Struct*. 2025;1328:141325. https://doi.org/10.1016/j.molstruc.2025.141325.
10) Kaddouri Y, Abrigach F, Mechbal N, Karzazi Y, Kodadi ME, Aouniti A, et al. Pyrazole compounds: Synthesis, molecular structure, chemical reactivity, experimental and theoretical DFT FTIR spectra. *Mater Today Proc*. 2019;13(3):956–963. https://doi.org/10.1016/j.matpr.2019.04.060.
11) Tüz B. Investigation of pyrazolyl derivatives Schiff base ligands and their metal complexes used as anti-cancer drug. *Spectrochim Acta A Mol Biomol Spectrosc*;227:117663. https://doi.org/10.1016/j.saa.2019.117663.
12) Hosny NM, Belal A, Motawea R, Hussien MA, Abdel-Rhman MH. Spectral characterization, DFT, docking and cytotoxicity of N-benzyl-4,5-dihydro-3-methyl-5-oxo-1H-pyrazole-4-carbothioamide and its metal complexes. *J Mol Struct*. 2021;1232:130020. https://doi.org/10.1016/j.molstruc.2021.130020.
13) Aftab A, Shaheer M, Garg N, et al. Probing the chemical landscape of 3,4-dichloro-1,2,5-thiadiazole: DFT calculations and biological activity insights. *Spectrosc Lett*. 2025;p. 1–22. https://doi.org/10.1080/00387010.2024.2448289.
14) Aroua LM, Alkhaibari IS, Alminderej FM, Messaoudi S, Chigurupati S, Al-mahmoud SA, et al. Synthesis, bioactivity, and molecular docking of pyrazole bearing Schiff-bases as prospective dual alpha-amylase and alpha-glucosidase inhibitors with antioxidant activity. *J Mol Struct*. 2025;1320:139291.

https://doi.org/10.1016/j.molstruc.2024.139291.
15) Zeyrek CT, Akman S, Ilhan IO, Kökbudak Z, Sarıpınar E, Akkoc S. Experimental and theoretical studies on 3-(4-chlorophenyl)-5-(4-ethoxyphenyl)-4,5-dihydropyrazole-1-carbonitrile: DFT quantum mechanical calculation, vibrational band analysis, prediction of activity spectra, and molecular docking. *J Mol Struct*. 2023;1276:134773. https://doi.org/10.1016/j.molstruc.2022.134773.
16) Hehre T, Klunzinger P, Deppmeier B, Ohlinger W, Hehre W. Accurate prediction of ωB97X-D/6-31G* equilibrium geometries from a neural net starting from Merck molecular force field (MMFF) molecular mechanics geometries. *J Chem Inf Model*. 2025;65(5):2314–2321. https://doi.org/10.1021/acs.jcim.4c01898.
17) Premalatha M, Anitha K, Revathi B, Balachandran V, Narayana B, Jayashree A, et al. Delving into 5-Amino-3-(4-chlorophenyl)-1-isonicotinoyl-2,3-dihydro-1H-pyrazole-4-carbonitrile ligand: Synthesis, spectroscopic (FT-IR, FT-Raman, NMR, UV-Vis), reactivity (ELF, LOL and Fukui), NCI, molecular docking and in silico ADMET studies by experimental and DFT methods. *J Mol Struct*. 2024;1316:138772. https://doi.org/10.1016/j.molstruc.2024.138772.
18) Shanmugapriya N, Balachandran V, Revathi B, Narayana B, Salian VV, Vanasundari K, et al. Quantum chemical calculation, performance of selective antimicrobial activity using molecular docking analysis, RDG and experimental (FT-IR, FT-Raman) investigation of 4-[{2-[3-(4-chlorophenyl)-5-(4-propan-2-yl) phenyl)-4, 5-dihydro-1H-pyrazol-1-yl]-4-oxo-1, 3-thiazol-5(4H)-ylidene} methyl] benzonitrile. *Heliyon*. 2021;7:e07634. https://doi.org/10.1016/j.heliyon.2021.e07634.
19) Koca I, Yakan M, Çapan İ, Şahin E, Sert Y. Experimental and computational studies of 1,5-diphenyl-pyrazole-3-carboxamide compounds as potential Cannabinoid receptor type 1. *J Mol Struct*. 2022;1264:133269. https://doi.org/10.1016/j.molstruc.2022.133269.
20) Filho EV, Pinheiro EMC, Pinheiro S, Greco SJ. Aminopyrimidines: Recent synthetic procedures and anticancer activities. *Tetrahedron*. 2021;92:132256. https://doi.org/10.1016/j.tet.2021.132256.
21) Nagalakshmi R, Balachandran V, Viji A, Narayana B, Alharethy F, Murugan R, et al. Quantum chemical calculations and molecular docking studies of 5-amino-3-(2,5-dimethoxyphenyl)-1-isonicotinoyl-2,3-dihydro-1H-pyrazole-4-carbonitrile. *Zeitschrift für Physikalische Chemie*. https://doi.org/10.1515/zpch-2024-0750.
22) Sivakumar C, Revathi B, Balachandran V, Narayana B, Salian VV, Shanmugapriya N, et al. Molecular structure, spectroscopic, quantum chemical, topological, molecular docking and antimicrobial activity of 3-(4-Chlorophenyl)-5-[4-propan-2-yl) phenyl-4, 5-dihydro-1H-pyrazol-1-yl] (pyridin-4-yl) methanone. *J Mol Struct*. 2021;1224:129286. https://doi.org/10.1016/j.molstruc.2020.129286.
23) Sivakumar C, Balachandran V, Narayana B, Salian VV, Revathi B, Shanmugapriya N, et al. Molecular spectroscopic assembly of 3-(4-chlorophenyl)-5-[4-(propane-2-yl) phenyl] 4, 5-dihydro-1H pyrazole-1-carbothioamide, antimicrobial potential and molecular docking analysis. *J Mol Struct*. 2020;1210:128005. https://doi.org/10.1016/j.molstruc.2020.128005.
24) Hiremath SM. Vibrational, electronic and reactivity insight on (5-chloro-benzofuran-3-yl)-acetic acid hydrazide: A Spectroscopic and DFT approach. *J Mol Struct*. 2021;p. 130479. https://doi.org/10.1016/j.molstruc.2021.130479.